Relativistic semiempirical-core-potential calculations of Sr^+ using Laguerre and Slater spinors

Jun Jiang*
Key Laboratory of Atomic and Molecular Physics and Functional Materials of Gansu Province, College of Physics and Electronic Engineering, Northwest Normal University, Lanzhou 730070, People's Republic of China

J. Mitroy†
School of Engineering, Charles Darwin University, Darwin NT 0909, Australia

Yongjun Cheng
Academy of Fundamental and Interdisciplinary Science, Harbin Institute of Technology, Harbin 150080, People's Republic of China and School of Engineering, Charles Darwin University, Darwin NT 0909, Australia

Michael W. J. Bromley‡
School of Mathematics and Physics, The University of Queensland, Brisbane, Queensland 4075, Australia
(Received 17 May 2016; published 23 December 2016)

A relativistic description of the structure of heavy alkali-metal atoms and alkali-like ions using S-spinors and L-spinors is developed. The core wave function is defined by a Dirac-Fock calculation using an S-spinor basis. The S-spinor basis is then supplemented with a large set of L-spinors for calculation of the valence wave function in a frozen-core model. The numerical stability of the L-spinor approach is demonstrated by computing the energies and decay rates of several low-lying hydrogen eigenstates, along with the polarizabilities of a $Z = 60$ hydrogenic ion. The approach is then applied to calculate the dynamic polarizabilities of the $5s$, $4d$, and $5p$ states of Sr^+. The magic wavelengths at which the Stark shifts between different pairs of transitions are 0 are computed. Determination of the magic wavelengths for the $5s \rightarrow 4d_{\frac{3}{2}}$ and $5s \rightarrow 4d_{\frac{5}{2}}$ transitions near 417 nm (near the wavelength for the $5s \rightarrow 5p_j$ transitions) would allow determination of the oscillator strength ratio for the $5s \rightarrow 5p_{\frac{1}{2}}$ and $5s \rightarrow 5p_{\frac{3}{2}}$ transitions.

DOI: 10.1103/PhysRevA.94.062514

I. INTRODUCTION

This paper describes the development and application of a relativistic model for atomic structure. The basic strategy of the model is to partition the atom into valence and core electrons. The core electrons are represented by orbitals obtained from Dirac-Fock (DF) calculations. The wave function for the valence electrons is computed by expanding the wave function as a linear combination of Laguerre function spinors (L-spinors) and Slater function spinors (S-spinors) [1–3]. The direct and exchange interactions between the core and the valence electrons can be computed without approximation. Core-valence correlations can be represented by simply introducing semiempirical core polarization potentials, which are tuned to ensure that the energies for the valence electrons agree with experiments [4–6].

The motivation for this methodology is based on the success of similar methodologies in computing the atomic properties of light atoms, namely, a nonrelativistic configuration interaction with a semiempirical-core-potential method (CICP) [4–7]. As a recent example, the dipole polarizability of the Si^{2+} ion computed with a similar methodology is 11.688 a_0^3 [8]. An analysis of a resonant excitation stark ionization spectroscopy [9] experiment give 11.669(9) a_0^3 [8,10], while a very sophisticated relativistic configuration interaction using many-body perturbation theory (MBPT) calculation gave 11.670(13) a_0^3 [11]. Numerous other examples of very good agreement of the semiempirical method with the most advanced *ab initio* theoretical models for oscillator strengths and polarizabilities can be found in Refs. [12–14].

There are a number of reasons for the success of the relativistic semiempirical approach. First, this approach is based on the *ab initio* DF calculation to define the core. Second, tuning energies to experimental values leads to wave functions that have the correct asymptotic decay at long distances from the nucleus. The multipole matrix elements needed for oscillator strength and polarizability calculations tend to be dominated by the large-r form of the wave function. Finally, partitioning the wave function into frozen-core electrons and an active valence electron reduces the equation for the wave function and energies into one equation that admits a close to exact numerical solution, here using a large (orthogonal) Laguerre basis.

It should be noted that the DF + core-polarization method adopted here has been extensively used by Migdalek and co-workers to calculate the oscillator strengths of many atoms [15–18]. They solved the radial equations numerically [19], and they typically restricted their transitions to between those of the low-lying states. A B-spline DF + core-polarization method has also been developed by Tang *et al.* [20] and the atomic properties of Ca^+ have been calculated.

The present work gives a brief description of the strategy adopted to convert an existing nonrelativistic Hartree-Fock

*phyjiang@yeah.net
†Deceased.
‡http://www.smp.uq.edu.au/staff/brom

(HF) program [21] into a relativistic DF program. Next, the technical details on performing calculations for one-valence-electron atoms and ions are discussed. These methods are then applied to the solution of hydrogen and hydrogenic atoms as a test for evaluation. We employ S-spinor and L-spinor basis sets, which enables the calculation of transition matrix elements between both the bound states and the continuum states (pseudostates). This enables us here to compute atomic polarizabilities [22], where the continuum makes a significant contribution [6].

The main results presented are the oscillator strengths and static and dynamic polarizabilities for the low-lying states of Sr^+ ions. In addition, some of the magic wavelengths for $5s$-$5p_J$ and $5s$-$4d_J$ transitions are presented, at which the ac-Stark shift of the transition energy is 0. The static polarizabilities of Sr^+ can be used to estimate the frequency shifts of $5s$-$4d_J$ clock transitions due to background fields such as blackbody radiation shifts [23]. The magic wavelengths can be used, for example, for high-precision trapping measurements [24,25]

II. FORMULATION AND VALIDATIONS

The single-electron Dirac equation can be written as

$$H\Psi(\mathbf{r}) = E\Psi(\mathbf{r}), \tag{1}$$

where the Hamiltonian

$$H = c\boldsymbol{\alpha}\cdot\boldsymbol{p} + \beta c^2 - \frac{Z}{r} + V_{\rm core}, \tag{2}$$

$\boldsymbol{p}$ is the momentum operator, and $\boldsymbol{\alpha}$ and β are 4×4 matrices of the Dirac operators [26]. The $V_{\rm core}$ represents the valence electron–core electron interaction and is described shortly.

Here we present the first results for two separate codes. The first is the DF calculation, which generates the closed-shell orbitals using purely Slater-type orbitals (STOs). The second code solves for a single valence electron orbiting the closed shell using a mixture of the STOs produced by the first code and additional Laguerre-type orbitals to describe the valence electronic structure and continuum physics.

A. Calculations of core orbitals

The starting point of a calculation involving closed shells is the DF calculation for the core state of the atoms. The DF equations are closely related to the HF equations. The atomic Schrödinger Hamiltonian is replaced by the Dirac-Coulomb Hamiltonian and the single-particle orbitals are now four-component spinors with a large and a small component.

The strategy used to generate a DF wave function is to adapt an existing HF program [21] which expands the orbitals as a linear combination of Slater (or Gaussian)-type orbitals. The first stage of the modification is to generate the angular representation of the orbitals from the $\ell \rightarrow \ell, j$ representation.

The next stage is to write each orbital in terms of S-spinors. Each orbital wave function can be written as

$$\psi_{n\kappa m}(\mathbf{r}) = \frac{1}{r}\begin{pmatrix} P_{n\kappa}(r)\Omega_{\kappa m}(\hat{\mathbf{r}}) \\ i\,Q_{n\kappa}(r)\Omega_{-\kappa m}(\hat{\mathbf{r}})\end{pmatrix}, \tag{3}$$

where κ is the relativistic angular quantum number, which is connected to the total angular momentum quantum number j and the orbital angular momentum quantum number ℓ,

$$\kappa = \ell(\ell+1) - j(j+1) - \tfrac{1}{4}. \tag{4}$$

$P_{n\kappa}(r)$ and $Q_{n\kappa}(r)$ represent the large and small components of the radial wave function, and $\Omega_{\kappa m}(\hat{\mathbf{r}})$ and $\Omega_{-\kappa m}(\hat{\mathbf{r}})$ are the angular components.

The radial wave functions $P_{n\kappa}(r)$ and $Q_{n\kappa}(r)$ are expanded as N terms in an S-spinor basis

$$P_{n\kappa}(r) = \sum_{i=1}^{N} p_i \phi^P_{i,\kappa}(r), \quad Q_{n\kappa}(r) = \sum_{i=1}^{N} q_i \phi^Q_{i,\kappa}(r), \tag{5}$$

where the superscript P and Q identify the "large" and "small" components of the Dirac spinor in a conventional way.

It is common to formally subdivide the basis functions into small- and large-type functions and explicitly recognize this when casting the DF equations into operational form [3]. In the present code, we define each S-spinor term as an orbital, and each orbital has a label identifying it as being of a large or a small component. These labels are taken into account when computing the matrix elements of the DF Hamiltonian. This makes minimal modifications to those parts of the program that construct and diagonalize the Hamiltonian. In effect, information about the spinor construction is confined to those parts of the program that evaluate the matrix elements of the basis functions.

S-spinors are generalizations of Slater-type orbitals adapted to relativistic systems. The first modification is the inclusion of a radial r^γ prefactor with

$$\gamma(\kappa) = \sqrt{\kappa^2 - Z^2/c^2} \tag{6}$$

to ensure that these functions have the correct asymptotic form at origin. Here, Z is the atomic number and we adopt $c = 137.035\,999\,1$ as the speed of light (in atomic units).

The second modification includes choosing the large- and small-component basis functions to approximately satisfy the kinetic balance condition [2]. The unnormalized radial components are written as

$$\phi^{P,Q}_{i,\kappa}(r) = r^\gamma e^{-\lambda_i r} \tag{7}$$

for orbitals with $\kappa < 0$ and

$$\phi^{P,Q}_{i,\kappa}(r) = A_{P,Q} r^\gamma e^{-\lambda_i r} + \lambda r^{\gamma+1} e^{-\lambda_i r} \tag{8}$$

for orbitals with $\kappa > 0$, where

$$A_P = \frac{(\kappa + 1 - \sqrt{\kappa^2 + 2\gamma + 1})(2\gamma+1)}{2(\sqrt{\kappa^2+2\gamma+1} - \kappa)} \tag{9}$$

for the large components and

$$A_Q = \frac{(\kappa - 1 - \sqrt{\kappa^2 + 2\gamma + 1})(2\gamma+1)}{2(\sqrt{\kappa^2+2\gamma+1} - \kappa)} \tag{10}$$

for the small components.

1. *Numerical test: Energy of closed-shell atoms*

A DF basis set is formed as a collection of S-spinors with positive real exponents $\{\lambda_i\}$ and coefficients $\{p_i\}$ and $\{q_i\} \forall i = 1,2,\ldots,N_S$, which undergo variational optimization. The S-spinor for the orbitals with $\kappa < 0$ has a very simple form.

TABLE I. Comparison of numerical DF energies (in a.u.) of several closed-shell atoms and ions as computed with various S-spinor basis sets using the present S-spinor program and the GRASP92/2K [28,29] and DBSR_HF [30] programs. The notation $a[b]$ indicates $a \times 10^b$. Underscores denote digits which differ between the two programs.

Atom/ion	Basis set	S-spinor	GRASP92/2K	DBSR_HF [30]
Li^+	$7s$	−7.23720552	−7.23720552	−7.23720552
Na^+	$10s,8p$	−1.61895967[2]	−1.61895968[2]	−1.61895968[2]
K^+	$12s,10p$	−6.01379051[2]	−6.01379058[2]	−6.01379059[2]
Rb^+	$11s,8p,5d$	−2.97969323[3]	−2.97969324[3]	−2.97969325[3]
Cs^+	$14s,12p,10d$	−7.78694367[3]	−7.78694284[3]	−7.78694285[3]
Ne	$10s,8p$	−1.28691968[2]	−1.28691970[2]	−1.28691969[2]
Ar	$11s,9p$	−5.28684446[2]	−5.28684451[2]	−5.28684450[2]
Kr	$10s,9p,5d$	−2.78888845[3]	−2.78888486[3]	−2.78888483[3]
Xe	$14s,13p,9d$	−7.44716330[3]	−7.44716272[3]	−7.44716273[3]
Be^{2+}	$7s$	−1.36140010[1]	−1.36140014[1]	−1.36140014[1]
Mg^{2+}	$10s,7p$	−1.99150128[2]	−1.99150137[2]	−1.99150137[2]
Ca^{2+}	$14s,11p$	−6.79105063[2]	−6.79105063[2]	−6.79105064[2]
Sr^{2+}	$12s,10p,5d$	−3.17755410[3]	−3.17755410[3]	−3.17755410[3]
Ba^{2+}	$15s,14p,10d$	−8.13548402[3]	−8.13548296[3]	−8.13548296[3]

The radial prefactor does not allow for additional powers of r as prefactors. This is distinct from the related STO basis sets used for nonrelativistic calculations, which usually have radial prefactors with a variety of powers of r [27]. In our calculations, the S-spinor basis sets used are based on nonrelativistic basis sets. An STO basis with all functions restricted to $n = \ell + 1$ was optimized for the nonrelativistic calculation. Once the optimization was complete, this was modified by the replacement $n \to \sqrt{\kappa^2 - Z^2/c^2}$ for S-spinors. This is based on the form of the exact wave functions for $\kappa < 0$. No further minor optimization is undertaken, as the relativistic self-consistent field calculations are time-consuming.

Table I lists DF energies computed using S-spinor basis and numerical DF energies computed using GRASP92/2K [28,29] and the B-spline DF program (DBSF_HF) [30]. For the light atoms, the three sets of energies are in very good agreement with each other. For Cs^+, Kr, Xe, and Ba^{2+}, heavy atoms, the present S-spinor energies are lower than the energies from GRASP92/2K [28,29] and DBSF_HF [30]. See Supplemental Tables I–III for lists of basis exponents [31].

TABLE II. Theoretical (RCICP) energies (ε in Hartree) and separated mass-corrected $E1$ ($\Gamma^{E(1)}$) and $E2$ ($\Gamma^{E(2)}$) decay rates (in seconds $^{-1}$) for several eigenstates of hydrogen. Underscores of the calculated energies (ε_I) denote digits which are different from the exact value [37]. η is the reduced mass of hydrogen and m_e is the mass of the electron. Experimental (expt.) values of $\Gamma^{E(1)}$ are taken from the NIST tabulation [38]. The notation $a[b]$ indicates $a \times 10^b$.

I	j_I	ε_I	$\Gamma_I^{E(1)} \times \eta/m_e$	$\Gamma_I^{E(1)}$ (expt. [38])	$\Gamma_I^{E(2)} \times \eta/m_e$
$1s$	$\frac{1}{2}$	−0.5000066565917	–	–	–
$2s$	$\frac{1}{2}$	−0.125002080201	–	–	–
$2p$	$\frac{1}{2}$	−0.125002080168	6.26490[8]	6.2649[8]	–
	$\frac{3}{2}$	−0.125000416023 4	6.26497[8]	6.2648[8]	1.303[−22]
$3s$	$\frac{1}{2}$	−0.055556295195	6.31427[6]	6.3143[6]	–
$3p$	$\frac{1}{2}$	−0.055556295175	1.89698[8]	1.8970[8]	23.9082
	$\frac{3}{2}$	−0.055555802098 1	1.89704[8]	1.8970[8]	23.9084
$3d$	$\frac{3}{2}$	−0.055555802091 83	6.46522[7]	6.4653[7]	644.766
	$\frac{5}{2}$	−0.055555637726	6.46512[7]	6.4651[7]	644.774
$4s$	$\frac{1}{2}$	−0.031250338027 5	4.41402[6]	4.4140[6]	1.02820
$4p$	$\frac{1}{2}$	−0.031250338020 4	8.12658[7]	8.1267[7]	12.8460
	$\frac{3}{2}$	−0.031250130012 6	8.12687[7]	8.1267[7]	12.8464
$4d$	$\frac{3}{2}$	−0.031250130018 6	2.76633[7]	2.7663[7]	336.889
	$\frac{5}{2}$	−0.031250060663	2.76628[7]	2.7663[7]	336.895
$4f$	$\frac{7}{2}$	−0.031250060671	1.37880[7]	1.3788[7]	67.5649
	$\frac{5}{2}$	−0.031250025993	1.37879[7]	1.3788[7]	67.5646

TABLE III. Cutoff parameters, $\rho_{\ell j}$, of the core polarization potential for an electron-Sr^{2+} interaction.

ℓ	j	$\rho_{\ell j}$ (units of a_0)	j	$\rho_{\ell j}$ (units of a_0)
s	$\frac{1}{2}$	2.04960	–	–
p	$\frac{1}{2}$	1.97169	$\frac{3}{2}$	1.97600
d	$\frac{3}{2}$	2.35353	$\frac{5}{2}$	2.36534
f	$\frac{5}{2}$	2.15023	$\frac{7}{2}$	2.19469

B. Calculation of valence orbitals

The orbitals for the valence electrons are written as linear combinations of S-spinors and L-spinors. L-spinors are generalizations of Laguerre-type orbitals [32] adapted to relativistic systems, and they are derived from the relativistic analogues of Coulomb Sturmians [2]. The (unnormalized) L-spinors are written as

$$\phi^P_{i,\kappa}(r) = r^\gamma e^{-\lambda_i r}\left\{(\delta_{n_i,0}-1)L^{2\gamma}_{n_i-1}(2\lambda_i r) + BL^{2\gamma}_{n_i}(2\lambda_i r)\right\} \tag{11}$$

and

$$\phi^Q_{i,\kappa}(r) = r^\gamma e^{-\lambda_i r}\left\{(\delta_{n_i,0}-1)L^{2\gamma}_{n_i-1}(2\lambda_i r) - BL^{2\gamma}_{n_i}(2\lambda_i r)\right\}, \tag{12}$$

where the balanced coefficient

$$B = \frac{\sqrt{n_i^2 + 2n_i\gamma + \kappa^2} - \kappa}{n_i + 2\gamma}, \tag{13}$$

with n_i being a non-negative integer ($n_i \geq 0$ for $\kappa < 0$ and $n_i \geq 1$ for $\kappa > 0$). The L^α_n are Laguerre polynomials [33], which are computed using the recursion relation

$$L^\alpha_{n+1}(x) = \frac{(2n+\alpha+1-x)}{(n+1)}L^\alpha_n(x) - \frac{(n+\alpha)}{(n+1)}L^\alpha_{n-1}(x), \tag{14}$$

with $L^\alpha_0(x) = 1$ and $L^\alpha_1(x) = 1+\alpha-x$. In our single-valence electron calculations, we always choose $2N$ L-spinor orbitals which include N large-component orbitals and N small-component orbitals.

The radial Dirac equation, Eq. (1), can be solved as a (real, symmetric) matrix eigenproblem, with the resulting set of N eigenfunctions

$$\Psi_I(\mathbf{r}) = \sum_{n_I=1}^{N} c_{n_I}\psi_{n_I\kappa_I m_I}(\mathbf{r}), \tag{15}$$

where $I \in 1,\ldots,N$. In order to compare with nonrelativistic calculations, we replace the energy E with $\varepsilon = E - mc^2$, where m is the mass of the electron ($m = 1$ in atomic units).

1. Numerical test: Energy of the hydrogen atom

Our code was first tested by diagonalizing the ground state of hydrogen (i.e., $Z = 1$, $V_{\rm core} = 0$) with $N = 50$ L-spinors. A value of $\lambda = 2.0$ was chosen for the s orbitals and $\lambda = 1.0$ for other orbitals ($\lambda = 1.0$ would correspond to the exact hydrogen ground state).

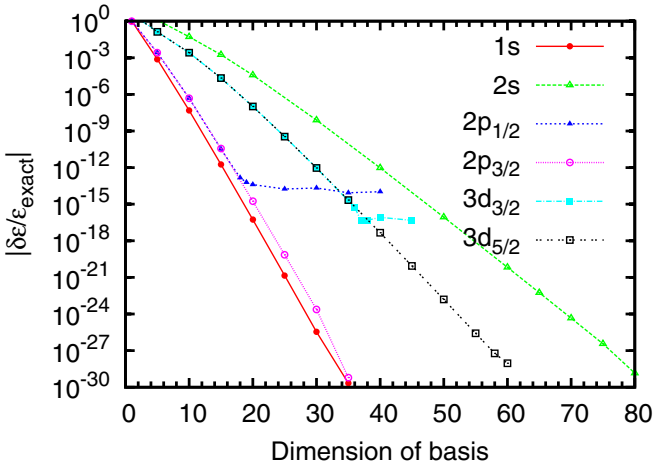

FIG. 1. Convergence of the energy of the low-lying hydrogen eigenstates relative to the exact energy $\delta_\varepsilon/\varepsilon_{\rm exact} = (\varepsilon - \varepsilon_{\rm exact})/\varepsilon_{\rm exact}$ as the dimension of the L-spinor basis is increased. The exponent in the L-spinor basis was set to $\lambda = 2.0$.

However, we can also compare the basis-set convergence of the eigenenergy to the exact solution of the Dirac equation. For states with $\kappa > 0$ ($2s_{\frac{1}{2}}, 2p_{\frac{3}{2}}, 3d_{\frac{5}{2}}$) the convergence patterns are all monotonic as shown in Fig. 1. Convergence is rapid and an accuracy of about 10^{-30} is the achievable limit with quadruple-precision arithmetic.

The convergence of the eigenenergy for the $2p_{\frac{1}{2}}$ and $3d_{\frac{3}{2}}$ states with increasing dimension of the L-spinor basis stalled at some point, as also shown in Fig. 1. The $2p_{\frac{1}{2}}$ energy using the L-spinor representation actually goes below that of the exact energy at $N = 20$ by 5×10^{-15} Hartree. This is suspicious of a double precision limitation inside the code for $\kappa < 0$ states. However, despite experimentation with both EISPACK and LAPACK eigensolvers we were unable to push below that of a purely double precision calculation. Thus, the remainder of the Sr^+ calculations shown in this paper are all computed in double precision, where the uncertainties relating to the core potential lie far above the limits established here.

C. Calculation of transition matrix elements

The 2^k-pole oscillator strength, $f^{(k)}_{IJ}$, from initial state Ψ_I to another eigenstate Ψ_J is defined as

$$f^{(k)}_{IJ} = \frac{2\varepsilon_{IJ}|\langle\Psi_I\|r^k\mathbf{C}^{(k)}(\hat{\mathbf{r}})\|\Psi_J\rangle|^2}{(2k+1)(2j_I+1)}, \tag{16}$$

with $\varepsilon_{IJ} = E_J - E_I$ being the excitation energy, j_I is the total angular momentum for the initial state, and $\mathbf{C}^{(k)}(\hat{\mathbf{r}})$ is the k-th order spherical tensor. The line strength, $S^{(k)}_{IJ} = |\langle\Psi_I\|r^k\mathbf{C}^{(k)}(\hat{\mathbf{r}})\|\Psi_J\rangle|^2 = |R^{(k)}_{IJ}|^2$, is calculated via the reduced matrix elements, $R^{(k)}_{IJ}$, between the orbitals

$$\begin{aligned} R^{(k)}_{IJ} &= \langle\Psi_I\|r^k\mathbf{C}^{(k)}(\hat{\mathbf{r}})\|\Psi_J\rangle \\ &= \sum_{n_I,n_J} c_{n_I}c_{n_J}\langle\psi_{n_I}\|r^k\mathbf{C}^{(k)}(\hat{\mathbf{r}})\|\psi_{n_J}\rangle, \end{aligned} \tag{17}$$

whose (orbital) matrix elements split into a radial part

$$\langle\psi_{n_I}(r)|r^k|\psi_{n_J}(r)\rangle = \int_0^\infty \frac{r^k}{r^2}\big[P_{n_I}(r)P_{n_J}(r) + Q_{n_I}(r)Q_{n_J}(r)\big]r^2dr, \quad (18)$$

multiplied by an angular part [3]

$$\langle\Omega_{\kappa_I}(\hat{\mathbf{r}})\|\mathbf{C}^{(k)}\|\Omega_{\kappa_J}(\hat{\mathbf{r}})\rangle = (-1)^{j_I+\frac{1}{2}}\sqrt{(2j_I+1)(2j_J+1)} \times \begin{pmatrix} j_I & j_J & k \\ -\frac{1}{2} & \frac{1}{2} & 0 \end{pmatrix}. \quad (19)$$

1. Numerical test: Lifetimes of the hydrogen atom

The inverse lifetime of a state Ψ_I is computed as

$$\frac{1}{\tau_I} = \Gamma_I = \sum_{k=1}^{2}\Gamma_I^{\mathrm{E}(k)} = \sum_{k=1}^{2}\left(\sum_{J;E_J<E_I} A_{IJ}^{\mathrm{E}(k)}\right); \quad (20)$$

i.e., here the decay rate Γ_I consists only of $E1$ ($k=1$ dipole) and $E2$ ($k=2$ quadrupole) pathways. The transition probabilities, $A_{IJ}^{E(k)}$, can be written as [34,35]

$$A_{IJ}^{E(k)} = A_0\frac{A^{(k)}\varepsilon_{IJ}^{2k+1}}{(2j_I+1)c^{2k+1}}|\langle\Psi_I\|r^k\mathbf{C}^{(k)}(\hat{\mathbf{r}})\|\Psi_J\rangle|^2, \quad (21)$$

where the energy differences, the speed of light, and the matrix elements are given in atomic units. The SI unit conversion factor is the inverse of the atomic unit of time $A_0 = 4.134\,137\,333\,649\,3 \times 10^{16}$ Hz [36], and here the constants $A^{(1)} = 4/3$ and $A^{(2)} = 1/15$ [34,35]. The results of our calculations are listed in Table II. In the calculation here, the value $\lambda = 1.0$ was chosen for the s, p, d, and f orbitals, and calculations are computed in double precision. There are 9 or 10 significant digits that agree with the exact values [37] for the energies. In order to take account of the mass correction, the decay rates are multiplied by $\eta/m_e = 0.999\,455\,679\,517$, η is the reduced mass of hydrogen, and m_e is the mass of the electron. The dipole decay rates agree with the values in the National Institute of Science and Technology (NIST) database [38] very well.

D. Calculation of dynamic dipole polarizabilities

The dynamic dipole ($k=1$) polarizability for a state with angular momentum $j_I = \frac{1}{2}$ is independent of the magnetic projection m_I, while for $j_I > \frac{1}{2}$ it depends on m_I, i.e., via scalar ($\alpha_S^{(1)}$) and tensor ($\alpha_T^{(1)}$) components:

$$\alpha_I^{(1)}(\omega) = \alpha_{\mathrm{S}}^{(1)}(\omega) + \left(\frac{3m_I^2 - j_I(j_I+1)}{j_I(2j_I-1)}\right)\alpha_{\mathrm{T}}^{(1)}(\omega). \quad (22)$$

The 2^k-pole scalar polarizability is usually defined in terms of a sum over all intermediate states, excluding the initial state, while including the continuum [22],

$$\alpha_{\mathrm{S}}^{(k)}(\omega) = \sum_{J\neq I}^{N}\frac{f_{IJ}^{(k)}}{\varepsilon_{IJ}^2 - \omega^2}. \quad (23)$$

The expression for the tensor part of the dipole polarizability for a state I can be written as

$$\alpha_{\mathrm{T}}^{(1)}(\omega) = 6\sqrt{\frac{5j_I(2j_I-1)(2j_I+1)}{6(j_I+1)(2j_I+3)}} \times \sum_{J\neq I}^{N}(-1)^{j_I+j_J}\begin{Bmatrix} j_I & 1 & j_J \\ 1 & j_J & 2 \end{Bmatrix}\frac{f_{IJ}^{(1)}}{\varepsilon_{IJ}^2 - \omega^2}. \quad (24)$$

Of interest is mapping out the locations of "tune-out" wavelengths, ω_t [where $\alpha_I^{(1)}(\omega_t) \to 0$], and "magic" wavelengths, ω_m [where $(\alpha_I^{(1)}(\omega_m) - \alpha_J^{(1)}(\omega_m)) \to 0$] [22].

1. Numerical test: Polarizability of the $Z = 60$ ion

A benchmark test of the calculation is to compute the static dipole polarizability of hydrogenic ion ground states. The static dipole polarizability of the hydrogenic ground state for $Z = 60$ (excluding negative-energy states) is found to be $2.802\,469\,05 \times 10^{-7}$ a.u. This is in agreement to seven significant digits with a value computed recently using a B-spline basis [39]. When the negative-energy states are included, the dipole polarizability is found to be $2.797\,090\,6 \times 10^{-7}$ a.u. The same level of agreement is achieved compared with the value from the B-spline [39] and Lagrange-mesh method [40] and the Sturmian expansion of the generalized Dirac-Coulomb Green function [41]. Comparing with the above two values, we find that the contribution of negative-energy states to the polarizability is -5.3785×10^{-10} a.u., which is about 0.19% of the total polarizability. A similar degree of accuracy is achieved for the calculation of the quadrupole polarizability. The quadrupole polarizability of the hydrogenic ground state for $Z = 60$ (including negative-energy states) is found to be $2.371\,147\,054\,8 \times 10^{-10}$ a.u. This is in agreement to nine significant digits with the B-spline value [39] and the Sturmian expansion of the generalized Dirac-Coulomb Green function value [41].

III. ATOMIC PROPERTIES OF Sr^+

Having independently validated the operation of our two codes, we turn our attention to the computation of the challenging one-valence-electron ion, Sr^+, which requires the consequent usage of both codes. First, we outline our treatment of the core-valence interaction.

A. Calculation of the core-valence interaction

The interaction of the valence electron with the core electrons can be approximated as a direct and exchange potential, along with a core-polarization interaction:

$$\hat{V}_{\mathrm{core}} \approx \hat{V}_{\mathrm{dir}} + \hat{V}_{\mathrm{exc}} + \hat{V}_{p_1}. \quad (25)$$

A detailed description of the relevant one-body matrix elements can be found in Ref. [2]. In brief, the matrix elements of the direct interaction can be written as

$$\langle\psi_{n_I}|V_{\mathrm{dir}}|\psi_{n_J}\rangle = \delta_{\kappa_I,\kappa_J}\int_0^\infty \big(P_{n_I}(r)P_{n_J}(r) + Q_{n_I}(r)Q_{n_J}(r)\big)V_d(r)dr, \quad (26)$$

where the direct core potential acts locally and radially,

$$V_d(r) = \int_0^r \frac{\rho_{\rm core}(r')}{r} dr' + \int_r^\infty \frac{\rho_{\rm core}(r')}{r'} dr'. \quad (27)$$

$\rho_{\rm core}$ is the density of all of the core electrons, where

$$\rho_{\rm core}(r) = \sum_{c=1}^{N_{\rm core}} (2j_c+1)\big(P_c^2(r) + Q_c^2(r)\big). \quad (28)$$

$N_{\rm core}$ is the number of core orbitals (denoted by c) obtained from a preceding DF calculation (see Table I). The exchange matrix element between the ith and the jth valence electron and the core electrons can be written as a sum over the interaction with each core electron, *viz.*,

$$\langle\psi_i|V_{\rm exc}|\psi_j\rangle = -\delta_{\kappa_i,\kappa_j} \sum_{c=1}^{N_{\rm core}} \sum_k (2j_c+1) \times \begin{pmatrix} j_c & k & j_i \\ \frac{1}{2} & 0 & -\frac{1}{2} \end{pmatrix}^2 R^k(c,i,j,c), \quad (29)$$

where

$$R^k(a,b,c,d) = \int_0^\infty \int_0^\infty (P_a(r_1)P_c(r_1) + Q_a(r_1)Q_c(r_1)) \times \frac{r_<^k}{r_>^{k+1}} (P_b(r_2)P_d(r_2) + Q_b(r_2)Q_d(r_2)) dr_1 dr_2. \quad (30)$$

Here $r_<$ and $r_>$ are the lesser and greater of the distances r_1 and r_2 of the electrons, respectively (one of which here is a core electron). The radial integrals are computed numerically using Gaussian integration [32], which enables the mixed usage of Slater-type orbitals (to most compactly represent the core) and Laguerre-type orbitals (which are orthogonal and can thus be included towards completeness without linear dependence issues). In order to prevent the valence electrons collapsing into the core electron (S-spinor only) orbitals, a Gram-Schmidt orthogonalization of the orbital set is performed to ensure that all the electron orbitals are orthonormal.

B. Calculation of the semiempirical potential

The e^--Sr^{2+} one-body polarization potential V_{p1} is an extension of the semiempirical polarization potential used previously [34], here including the dipole, quadrupole, and octupole contributions as

$$V_{p1}(r) = -\sum_{k=1}^{3} \frac{\alpha_{\rm core}^{(k)}}{2r^{(2(k+1))}} \sum_{\ell,j} g_{k,\ell,j}^2(r) |\ell,j\rangle\langle\ell,j|. \quad (31)$$

Here, the factor $\alpha_{\rm core}^{(k)}$ is the static kth-order polarizability of the core electrons (obtained from independent calculations) and $g_{k,\ell,j}^2(r) = 1 - \exp(-r^{(2(k+2))}/\rho_{\ell,j}^{(2(k+2))})$ is a cutoff function designed to make the polarization potential finite at the origin, while we tune $\rho_{\ell,j}$ for each ℓ,j combination.

In our calculations, the core value adopted for the dipole is $\alpha_{\rm core}^{(1)} = 5.813$ a.u. [6,42], and that for the quadrupole is $\alpha_{\rm core}^{(2)} = 17.15$ a.u. [6,42], while that for the octupole is $\alpha_{\rm core}^{(3)} = 113$ a.u. [43]. The cutoff parameters for the polarization potentials are listed in Table III. These parameters are set by tuning the energy of the lowest state of each (ℓ,j) symmetry to the experimental value. The dipole transition matrix elements were computed with a modified transition operator [4,34,44,45], e.g.,

$$\mathbf{r} = \mathbf{r} - \alpha_{\rm core}^{(1)} \sqrt{1 - \exp(-r^6/\bar{\rho}^6)}\, \mathbf{r}/r^3. \quad (32)$$

The cutoff parameter $\bar{\rho}$ used in Eq. (32) was the average of the s, p, and d cutoff parameters (note that the weighting of the s was doubled to give it the same weighting as the two p and d orbitals).

1. *Results: Energies of* Sr^+

For the Sr^+ calculations we used the Laguerre parameters $\lambda = 1.6$ for s orbitals and $\lambda = 1.2$ for the others, with $N = 50$ orbitals for each angular momentum. The energies for a number of low-lying states are listed in Table IV. Compared with the experimental data taken from the NIST [38], we find that the error of the present calculations (labeled RCICP) is about 2×10^{-4} a.u. for the more highly excited s and p states and about five times as large for the d states. The $4d$ orbitals are undergoing the collapse for Sr^+ ions, and they are very sensitive to the choice of potential [46]. Although tuning the cutoff parameter for d orbitals takes the $4d$ energy to the experimental value, the $5d$ and $6d$ orbitals still differ greatly

TABLE IV. Theoretical (RCICP) and experimental energy levels (in Hartrees) for some of the low-lying states of Sr^+. Energies are given relative to the energy of the Sr^{2+} core. Experimental data are taken from the National Institute of Science and Technology (NIST) tabulation [38].

I	j	ε (RCICP)	ε (Expt.)	$\Delta\varepsilon$
$5s$	$\frac{1}{2}$	−0.4053555	−0.4053552	0.0000003
$4d$	$\frac{3}{2}$	−0.3390336	−0.3390336	0.0000000
	$\frac{5}{2}$	−0.3377563	−0.3377563	0.0000000
$5p$	$\frac{1}{2}$	−0.2973007	−0.2973008	0.0000001
	$\frac{3}{2}$	−0.2936464	−0.2936491	0.0000027
$6s$	$\frac{1}{2}$	−0.1875380	−0.1878515	0.0003135
$5d$	$\frac{3}{2}$	−0.1612581	−0.1625649	0.0013068
	$\frac{5}{2}$	−0.1608524	−0.1621700	0.0013176
$6p$	$\frac{1}{2}$	−0.1510966	−0.1512497	0.0001531
	$\frac{3}{2}$	−0.1497517	−0.1499367	0.0001850
$4f$	$\frac{7}{2}$	−0.1274645	−0.1274641	0.0000004
	$\frac{5}{2}$	−0.1274582	−0.1274582	0.0000000
$7s$	$\frac{1}{2}$	−0.1091774	−0.1093570	0.0001796
$6d$	$\frac{3}{2}$	−0.0969695	−0.0976983	0.0007288
	$\frac{5}{2}$	−0.0967790	−0.0975148	0.0007358
$7p$	$\frac{1}{2}$	−0.0923245	−0.0924291	0.0001046
	$\frac{3}{2}$	−0.0916778	−0.0918013	0.0001235
$5f$	$\frac{5}{2}$	−0.0815523	−0.0815557	0.0000034
	$\frac{7}{2}$	−0.0815463	−0.0815557	0.0000094
$5g$	$\frac{7}{2}$	−0.0802443	−0.0802252	0.0000191
	$\frac{9}{2}$	−0.0802442	−0.0802252	0.0000190

TABLE V. Comparison of reduced electric dipole ($E1$) and quadrupole ($E2$) line strengths for the principal transitions of Sr^+ with other calculations (MBPT-SD [43,47], CICP [34]). The (x) notation indicates the error in the last digits.

	RCICP	MBPT-SD	CICP
		Dipole	
$5s$-$5p_{\frac{1}{2}}$	9.285(140)	9.474(111)	9.2729
$5s$-$5p_{\frac{3}{2}}$	18.58(28)	18.93(22)	18.546
$5s$-$6p_{\frac{1}{2}}$	0.00203(64)	0.00063(10)	0.000158
$5s$-$6p_{\frac{3}{2}}$	0.00004(34)	0.00116(29)	0.000315
$5p_{\frac{1}{2}}$-$6s$	5.482(55)	5.434(65)	5.7963
$5p_{\frac{3}{2}}$-$6s$	11.90(11)	11.81(12)	11.593
$6s$-$6p_{\frac{1}{2}}$	42.68(17)	42.64(17)	42.414
$6s$-$6p_{\frac{3}{2}}$	84.39(31)	84.29(35)	84.827
$6p_{\frac{1}{2}}$-$7s$	22.76(9)	22.77(5)	23.964
$6p_{\frac{3}{2}}$-$7s$	49.13(9)	49.07(8)	47.928
$5p_{\frac{1}{2}}$-$5d_{\frac{3}{2}}$	17.95(75)	18.17(32)	18.724
$5p_{\frac{3}{2}}$-$5d_{\frac{3}{2}}$	3.816(15)	3.869(59)	3.7448
$5p_{\frac{3}{2}}$-$5d_{\frac{5}{2}}$	33.95(141)	34.40(57)	33.703
$4d_{\frac{3}{2}}$-$5p_{\frac{1}{2}}$	9.587(144)	9.685(181)	9.4865
$4d_{\frac{3}{2}}$-$5p_{\frac{3}{2}}$	1.901(29)	1.910(36)	1.8973
$4d_{\frac{5}{2}}$-$5p_{\frac{3}{2}}$	17.41(26)	17.53(31)	17.076
$4d_{\frac{3}{2}}$-$6p_{\frac{1}{2}}$	0.00121(412)	0.00608(257)	0.00225
$4d_{\frac{3}{2}}$-$6p_{\frac{3}{2}}$	0.00111(203)	0.00260(76)	0.000449
$4d_{\frac{5}{2}}$-$6p_{\frac{3}{2}}$	0.00757(165)	0.00202(58)	0.00404
$4d_{\frac{3}{2}}$-$4f_{\frac{5}{2}}$	8.582(129)	8.503(223)	8.6472
$4d_{\frac{5}{2}}$-$4f_{\frac{5}{2}}$	0.628(10)	0.623(14)	0.6177
$4d_{\frac{5}{2}}$-$4f_{\frac{7}{2}}$	12.54(19)	12.45(30)	12.353
		Quadrupole	
$5s$-$4d_{\frac{3}{2}}$	123.04(186)	123.94(87)	123.08
$5s$-$4d_{\frac{5}{2}}$	187.50(283)	188.98(140)	184.63

from the experiment. It is also shown in Table III that the cutoff parameters of d orbitals are larger than those of s, p and f orbitals, which results in weak polarization for the rest of the d orbitals.

By tuning the polarization potential cutoff parameters, the spin-orbit splittings are correct for the $4d_j$ and $5p_j$ levels. This also makes reasonably accurate spin-orbit splittings for the more highly excited states. For example, the present calculation of $6p_j$ splitting is 0.001 345 a.u., while the experimental splitting is 0.001 313 a.u. The $5d_j$ RCICP splitting is 0.000 406 a.u., while the experimental splitting is 0.000 395 a.u.

C. Line strengths and lifetimes

The line strengths for a number of low-lying transitions of Sr^+ are listed in Table V. Line strengths are mainly given for dipole transitions, while the exceptions are of the $5s \rightarrow 4d_j$ transitions. Table V lists the line strengths of the relativistic all-order single and double many-body perturbation theory (MBPT-SD) calculation [43,47]. Table V also lists the line strengths from a previous nonrelativistic calculation [34], labeled CICP, which can be regarded as a precursor to the present calculation.

The uncertainties of the present RCICP line strengths are also listed in Table V. The uncertainties of the matrix elements for the transitions between the $5s$, $5p$, $4d$, and $4f$ states are mainly caused by the frozen-core model since the correlation effects have been incorporated using the polarization potentials. This uncertainty was explored by an independent calculation using the GRASP2K program [29]. A complete calculation using the GRASP2K program is significantly time-consuming since the core-valence and core-core correlations should be included, and it is also restricted to limited transition processes. In the GRASP2K estimations here, just two kinds of single-configuration calculations were performed. One is the frozen-core calculation. In another calculation, all orbitals for the initial and final states were optimized separately and the orbital relaxation effects were included. These two quick GRASP2K calculations are compared with each other to indicate the uncertainties produced by the frozen-core approximation and the resultant differences are found to be smaller than 0.75%. Thus we set 0.75% as the uncertainties of the present RCICP matrix elements of the transitions between the $5s$, $5p$, $4d$, and $4f$ states.

The uncertainties of the matrix elements for the transitions of more highly excited states are estimated as the parametric functions of their binding energies. The functional form is

$$\delta R_{IJ} \approx \frac{\partial R_{IJ}}{\partial \varepsilon_I} \Delta\varepsilon_I + \frac{\partial R_{IJ}}{\partial \varepsilon_J} \Delta\varepsilon_J, \tag{33}$$

where R_{IJ} are their (reduced) matrix elements, and $\Delta\varepsilon$ values are listed in Table IV. The partial derivatives are evaluated by redoing the calculations with a slightly different polarization potential and checking the resultant change in the reduced matrix elements.

The nonrelativistic CICP radial matrix elements are the same for the different members of the same spin-orbit doublets. So the different line strengths are purely due to geometric factors related to the angular momentum of the states. The difference between the CICP and the present RCICP line strengths is typically small, not exceeding 6% for any of the strong transitions. Some of the differences that occur are due to the different energies of the spin-orbit doublets. The difference is about 0.1% for the resonance $5s \rightarrow 5p_j$ transitions. Differences can be larger for the weaker transitions with much lower line strengths, which are much more sensitive to small perturbations in the calculation of the matrix elements. The generally good agreement between the CICP and the RCICP matrix elements arises because both sets of calculations have their energies tuned to experimental values. The binding energy largely determines the long-range part of the wave function and it is this part of the wave function which dominates the calculation of the dipole and quadrupole matrix elements.

Our present RCICP calculations generally give improved results over our previous CICP calculations, compared with the MBPT-SD line strengths listed in Table V. We now see agreement at the level of a couple of percent between most of the RCICP and MBPT-SD line strengths, and most of our results lie within their error estimates. The RCICP line strengths are 2% lower than the MBPT-SD line strengths for the resonant $5s \rightarrow 5p_j$ transitions, although our results do lie outside their error estimates [43,47]. The two most

TABLE VI. Lifetimes (τ; in seconds) of the $4d_{\frac{3}{2}}$ and $4d_{\frac{5}{2}}$ levels of Sr^+. The $4d_{\frac{3}{2}}$:$4d_{\frac{5}{2}}$ lifetime ratios are also given.

Source	$\tau(4d_{\frac{3}{2}})$	$\tau(4d_{\frac{5}{2}})$	Ratio
RCICP	0.4442(67)	0.3974(59)	1.1176(341)
RCC [55]	0.426(8)	0.357(12)	1.193(65)
CICP [34]	0.443	0.404	1.0965
MBPT-SD [47]	0.441(3)	0.394(3)	1.119(14)
Expt. [56]		0.372(25)	
Expt. [54]	0.455(29)	0.408(22)	1.115(139)
Expt. [57,58]	0.435(4)	0.3908(16)	1.1131(68)

TABLE VIII. Pseudospectral oscillator strength distribution for the Sr^{2+} core. Energies are given in a.u.

i	Orbital	ε_i	f_i
1	$1s^2$	583.696	2
2	$2s^2$	80.400	2
3	$2p^6$	73.005	6
4	$3s^2$	13.484	2
5	$3p^6$	10.709	6
6	$3d^{10}$	5.703	10
7	$4s^2$	1.906	2
8	$4p^6$	1.108	6

egregious cases are the weak $5s$-$6p_{\frac{1}{2}}$ and $4d_{\frac{5}{2}}$-$6p_{\frac{3}{2}}$ transitions, which are around 200% different, even with the relatively large MBPT-SD error estimates taken into account. All of the >2% cases can be explained again due to the sensitivity to small perturbations in the calculations. The Sr^+ system presents an extreme benchmark challenge for all atomic structure methodologies.

Using the line strengths listed in Table V, the lifetimes of $4d_j$ and $5p_j$ states can be obtained using Eq. (21). Table VI gives the lifetimes of $4d_j$ states. The main contribution for the lifetimes of $4d_j$ comes from the $E2$ ($4d_j$-$5s$) transitions. The underlying theoretical frameworks of the relativistic coupled cluster (RCC) and MBPT-SD approaches have many common features [14,48,49]. In many instances, however, the atomic parameters computed using the RCC approach showed significant differences from other independent calculations [50–53]. This situation is also prevalent for the lifetime of the $4d_j$ states. The RCC lifetime ratio 1.1933 is 8% higher than that given by either the RCICP or the MBPT-SD calculation. The CICP lifetime ratio of 1.0965 is essentially due to the different energies of the two $4d_j$ states (since the matrix elements are the same in the CICP calculation). The RCICP lifetime ratio 1.1176 is in excellent agreement with the MBPT-SD ratio 1.1193 and the most recent experiment ratio 1.115 [54].

Different estimates of the $5p_j$ lifetimes are listed in Table VII. The $5p_j$ states have dipole transitions to two lower-lying states, namely, the $5s$ and $4d_j$ states. The transition to the $5s$ state is about 20 times larger than the transition to the $4d_j$ states. The RCICP and MBPT-SD lifetimes differ by 2% and the most precise experimental estimates obtained from laser excitation of ion beams [59,60] lie within the RCICP and MBPT-SD estimates. The RCC lifetimes are smaller than the RCICP and MBPT-SD results. The RCICP and MBPT-SD comparisons are reminiscent of the $4p_j$ lifetimes of Ca^+. In Ca^+ one finds that the RCICP lifetimes are about 2% larger than the MBPT-SD lifetimes [20]. The $5p_{\frac{1}{2}}$:$5p_{\frac{3}{2}}$ lifetime ratio agrees very well with experiments for both calculations.

D. Static polarizabilities

The scalar dipole polarizabilities include contribution from the core which is represented by a pseudo-oscillator strength distribution [6,62,63],

$$\alpha_S^{(\mathrm{core})}(\omega) = \sum_i^{N_C} \frac{f_i^{(1)}}{\varepsilon_i^2 - \omega^2}. \tag{34}$$

The pseudo-oscillator strength distribution is reported in Table VIII, using the number of electrons in each shell as the oscillator strength. Note that in the calculations of the polarizability difference for any two states, the core polarizabilities will effectively cancel each other.

The static dipole and quadrupole polarizabilities of the $5s$, $5p_j$, and $4d_j$ states are listed in Table IX. Once again, the overall agreement for the dipole polarizability between the RCICP and the MBPT-SD calculations is at the level of 1%–2%. The present calculations also agree with the all-order RCC method with the single and double approximation (RCC all-order) results. The RCICP ground-state dipole polarizability of 90.1 a.u. is about 2% smaller than the MBPT-SD polarizability. This is a direct consequence of the slightly different line strengths for the resonant transition in these two calculations, since the

TABLE VII. Lifetimes (τ; in nanoseconds) of the $5p_{\frac{1}{2}}$ and $5p_{\frac{3}{2}}$ states. The $5p_{\frac{1}{2}}$:$5p_{\frac{3}{2}}$ lifetime ratios are also listed. The quantity R is the fraction of the total decay rate arising from the indicated transition.

Level	RCICP	MBPT-SD [47]	RCC [61]	Expt. [59]	Expt. [60]
$\tau(5p_{\frac{1}{2}})$	7.523(112)	7.376	7.16	7.47(7)	7.39(7)
$R(5p_{\frac{1}{2}}$-$5s_{\frac{1}{2}})$	0.9439(282)	0.9444	0.9338		
$R(5p_{\frac{1}{2}}$-$4d_{\frac{1}{2}})$	0.0561(17)	0.0556	0.0662		
$\tau(5p_{\frac{3}{2}})$	6.773(100)	6.653	6.44	6.69(7)	6.63(7)
$R(5p_{\frac{3}{2}}$-$5s_{\frac{1}{2}})$	0.9394(281)	0.9400	0.9287		
$R(5p_{\frac{3}{2}}$-$4d_{\frac{3}{2}})$	0.0064(2)	0.0064	0.0075		
$R(5p_{\frac{3}{2}}$-$4d_{\frac{5}{2}})$	0.0542(16)	0.0536	0.0637		
$5p_{\frac{1}{2}}$:$5p_{\frac{3}{2}}$ ratio	1.111(18)	1.109	1.111	1.117(20)	1.114(20)

TABLE IX. Static ($\omega = 0$) scalar and tensor dipole polarizabilities, $\alpha_S^{(1)}$ and $\alpha_T^{(1)}$, and static quadrupole polarizabilities, $\alpha_S^{(2)}$, for low-lying states of the Sr^+ ion. All values are given in a.u.

State	Term	RCICP	Others	Ref. No. for others
$5s_{\frac{1}{2}}$	$\alpha_S^{(1)}$	90.10(127)	92.2(7)	MBPT-SD [43]
			91.30	MBPT-SD [47]
			90.54	RCC all-order [65]
			88.29	RCC [66]
			89.88	CICP [34]
			86(11)	Expt. [64]
	$\alpha_S^{(2)}$	1356.3(315)	1370.0(28)	MBPT-SD [43]
			1346	CICP [34]
$5p_{\frac{1}{2}}$	$\alpha_S^{(1)}$	−31.29(49)	−32.2(9)	MBPT-SD [43]
			−31.27	RCC all-order [65]
	$\alpha_S^{(2)}$	31596(455)		
$5p_{\frac{3}{2}}$	$\alpha_S^{(1)}$	−20.92(70)	−21.4(8)	MBPT-SD [43]
			−20.97	RCC all-order [65]
	$\alpha_T^{(1)}$	9.836(147)	10.74(23)	MBPT-SD [43]
			10.52	RCC all-order [65]
	$\alpha_S^{(2)}$	−13099(225)		
$4d_{\frac{3}{2}}$	$\alpha_S^{(1)}$	63.12(82)	63.3(9)	MBPT-SD [43]
			63.74	RCC all-order [65]
			61.43(52)	RCC [66]
	$\alpha_T^{(1)}$	−35.11(50)	−35.5(6)	MBPT-SD [43]
			−35.26	RCC all-order [65]
			−35.42(25)	RCC [66]
	$\alpha_S^{(2)}$	2713(44)		
$4d_{\frac{5}{2}}$	$\alpha_S^{(1)}$	61.99(72)	62.0(9)	MBPT-SD [43]
			62.08	RCC all-order [65]
			62.87(75)	RCC [66]
	$\alpha_T^{(1)}$	−47.38(67)	−47.7(8)	MBPT-SD [43]
			−47.35	RCC all-order [65]
			−48.83(25)	RCC [66]
	$\alpha_S^{(2)}$	−1728(23)		

energies of the lowest eigenstates have already been tuned to the experimental value and the slightly larger difference in the energies of the other excited states has a negligible effect on the polarizability. Only one experimental Sr^+ dipole polarizability has been obtained [64]. In that experiment, the energy differences between the $5snf$, $5sng$, $5snh$, and $5sni$ states of neutral strontium have been used to make an estimate of the Sr^+ core polarizability. However, the relatively large uncertainty of 13% cannot be used to discriminate between the different theoretical estimates.

The RCICP quadrupole polarizability of the ground state is about 1% smaller than the MBPT-SD polarizability. The nonrelativistic CICP calculation is 2% smaller than the MBPT-SD polarizability. This difference is a direct consequence of the difference in the underlying line strengths between the various calculations.

The RCICP dipole polarizabilities of $5p_j$ agree with the MBPT-SD polarizability very well. The dipole polarizabilities of $5p_j$ states are negative. This is because the downward transitions from $5p_j$ to $5s$ and $4d_j$ have very large negative oscillator strengths, which result in a negative polarizability. This is evident in Table XI (and Supplemental Tables IV and V [31]), which lists the contributions from different transitions to the polarizabilities. The tensor dipole polarizability of $5p_{\frac{3}{2}}$ from RCICP calculations is 8% smaller than that from MBPT-SD calculations. This is mainly because the matrix element of $5s \rightarrow 5p_{\frac{3}{2}}$ from the RCICP is samller than the MBPT-SD matrix element. The RCICP dipole scalar and tensor polarizabilities of $4d_j$ states agree with the MBPT-SD and RCC polarizabilities very well.

TABLE X. Differences in static dipole polarizabilities (in a.u.) for the $5s$-$4d_j$ transitions of the Sr^+ ion.

Method	$5s$-$4d_{\frac{5}{2}}$	$5s$-$4d_{\frac{3}{2}}$
RCICP	28.11(212)	27.00(214)
MBPT-SD [43]	30.2	28.9
RCC all-order [65]	28.46	26.8
RCC [66]	25.4	26.9
Expt. [23]	29.075(43)	

One important application of the polarizability is to give the magic wavelength by setting the difference between the polarizabilities of the two involved eigenstates to be 0. As an example, Table X lists the difference in static dipole polarizabilities for the $5s$ and $4d_j$ states. The polarizability difference between $5s$ and $4d_{\frac{5}{2}}$ is relevant to the determination of the error budget for the $5s \rightarrow 4d_{\frac{5}{2}}$ clock transition [24]. Until recently, the only estimates of the polarizability difference came from atomic structure calculations [34,47,66,67]. However, the scalar polarizability for this transition has recently been measured by utilizing the time-dilation effect [23]. The time dilation experiment gives a scalar polarizability difference that lies almost exactly halfway between the RCICP and the MBPT-SD polarizability differences.

TABLE XI. Contributions of individual transitions to the polarizabilities (in a.u.) of the $5s_{\frac{1}{2}}$ and $5p_{\frac{1}{2}}$ states for the static case and at the magic wavelengths. These results assume linearly polarized light. $\delta\lambda$ are uncertainties calculated by assuming that certain matrix elements have ±2% uncertainties.

ω (a.u.)	0	0.05961933
λ (nm)	∞	764.2378
$\delta\lambda$ (nm)		8
Ref. [65] (nm)		769.44
	$5s_{\frac{1}{2}}$	
$5p_{\frac{1}{2}}$	28.6439(4312)	41.1806
$5p_{\frac{3}{2}}$	55.4498(8348)	77.5362
Remainder	0.1891(28)	0.1918
Core	5.813[6,42]	5.8276
Total	90.0959(12688)	124.7362
	$5p_{\frac{1}{2}}$	
$5s_{\frac{1}{2}}$	−28.6439(4313)	−41.1806
$4d_{\frac{3}{2}}$	−76.5768(1.1530)	73.5687
$6s_{\frac{1}{2}}$	16.6954(1671)	23.7393
$5d_{\frac{3}{2}}$	44.4075(1.9050)	55.2192
Remainder	7.0082(1055)	7.5619
Core	5.813 [6,42]	5.8276
Total	−31.2971(4878)	124.7362

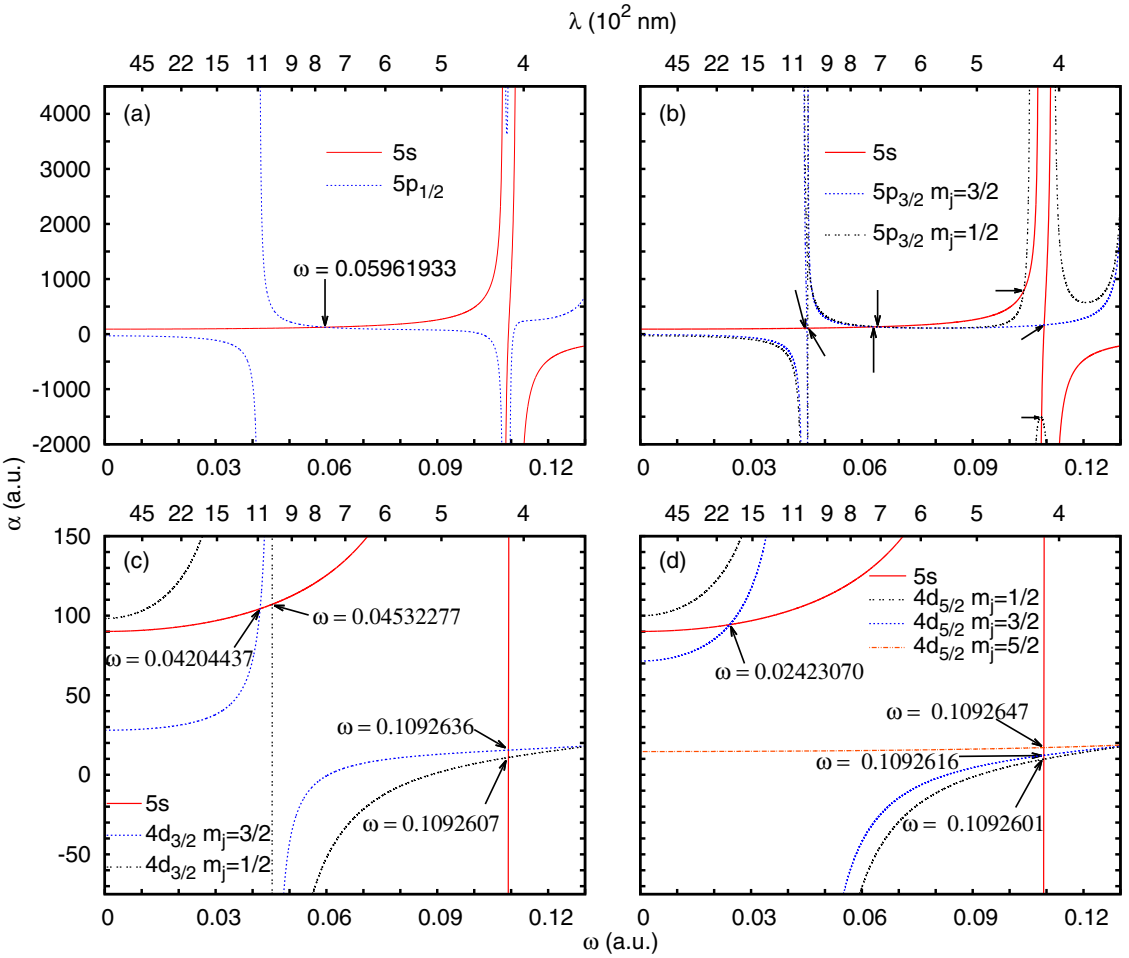

FIG. 2. Dynamic polarizabilities of various states of Sr^+. Comparison of (a) the $5s_{\frac{1}{2}}$ and $5p_{\frac{1}{2}}$ states, (b) $5s_{\frac{1}{2}}$ and $5p_{\frac{3}{2}}$, (c) $5s_{\frac{1}{2}}$ and $4d_{\frac{3}{2}}$, (d) and $5s_{\frac{1}{2}}$ and $4d_{\frac{5}{2}}$. The various magic wavelengths between the respective states are identified by arrows.

E. Dynamic polarizabilities and magic wavelengths

The Sr^+ dipole scalar and tensor dynamic polarizabilities are computed here as per Eq. (22), including the core contribution as per Eq. (34). The magic wavelength is calculated by setting the dynamical polarizability difference between the two involved eigenstates to be 0. An example breakdown for the $5s_{\frac{1}{2}}$ and $5p_{\frac{1}{2}}$ polarizabilities is reported for both the static case ($\omega = 0$) and at the first magic wavelength, $\omega = 0.059\,619\,33$ a.u., in Table XI.

The dynamic polarizabilities of the $5s_{\frac{1}{2}}$ and $5p_{\frac{1}{2}}$ states of Sr^+ are shown in Fig. 2(a). Note that these calculations assume linearly polarized light. The only magic wavelength for this transition for wavelengths greater than 400 nm occurs at $\lambda = 764.238$ nm ($\omega = 0.059\,619\,33$ a.u.). This occurs when the photon energy exceeds the energy for the $5p_{\frac{1}{2}}$-$4d_{\frac{3}{2}}$ transition. The $5s_{\frac{1}{2}}$ polarizability is found to be dominated by the $5s_{\frac{1}{2}}$-$5p_j$ transition, while the breakdown of the $5p_{\frac{1}{2}}$ polarizability reported in Table XI reveals that the transitions to the $5s$, $6s$, $4d_{\frac{3}{2}}$, and $5d_{\frac{3}{2}}$ states all make significant contributions to the $5p_{\frac{1}{2}}$ polarizability.

The dynamic polarizabilities of the $5s_{\frac{1}{2}}$ and $5p_{\frac{3}{2}}$ states of Sr^+ are in Fig. 2(b). Supplemental Tables IV and V [31] list the breakdown of the polarizabilities for the static case and at the magic wavelengths for both m_j values. There are seven magic wavelengths below $\omega = 0.110$ a.u. and four below 0.070 a.u.. Supplemental Tables IV and V [31] reveal that the positions of the magic wavelengths near 1004 and 1009 nm are strongly influenced by the relative sizes of the $5p_{\frac{3}{2}} \rightarrow 4d_{\frac{3}{2}}$ and $5p_{\frac{3}{2}} \rightarrow 4d_{\frac{5}{2}}$ line strengths. These two magic wavelengths occur when the photon energy lies between the transition energies of $5p_{\frac{3}{2}} \rightarrow 4d_{\frac{3}{2}}$ and $5p_{\frac{3}{2}} \rightarrow 4d_{\frac{5}{2}}$. Transitions to the $ns_{\frac{1}{2}}$ states make no contribution to the $5p_{\frac{3}{2},m=\frac{3}{2}}$ state polarizability for linearly polarized light. Combined with the experimental matrix elements of $5s \rightarrow 5p_j$ transitions, measurement of the 1009-nm magic wavelength would enable determination of the oscillator strength ratio of $f_{5p_{\frac{3}{2}} \rightarrow 4d_{\frac{3}{2}}} : f_{5p_{\frac{3}{2}} \rightarrow 4d_{\frac{5}{2}}}$. Suppose that all the remaining components of $5p_{\frac{3}{2}}$ polarizability including the $5p_{\frac{3}{2}} \rightarrow 5d_j$ contribution is 5%. Thus the overall uncertainty of the polarizability is less than 1%.

There are several other magic wavelengths worth mentioning. The magic wavelengths near 709 and 721 nm are caused by the gradual increase in the $5s_{\frac{1}{2}}$ polarizability as the photon energy approaches the $5s \rightarrow 5p_j$ excitation energy and the gradual decrease in the $5p_{\frac{3}{2}}$ polarizability as the energy becomes increasingly distant from the $5p_{\frac{3}{2}} \rightarrow 4d_j$ transition

energy. The magic wavelength at 438 nm for the $5p_{\frac{3}{2},m=\frac{1}{2}}$ magnetic sublevel is triggered by the polarizability associated with the $5p_{\frac{3}{2}} \rightarrow 6s$ transition. The magic wavelengths near 416 and 419 nm are caused by the rapid variation of the $5s$ polarizability for a photon energy lying between the excitation energies from $5s$ to $5p_{\frac{1}{2}}$ and $5p_{\frac{3}{2}}$ states. These magic wavelengths can give an estimate of the contribution to the $5p_{\frac{3}{2}}$ polarizability arising from excitations to the nd_j levels.

The dynamic polarizabilities of the $5s$ and $4d_{\frac{5}{2}}$ states are shown in Fig. 2(d), while Supplemental Table VI [31] lists the breakdown of the polarizabilities for the static case and at the magic wavelengths. This is probably the most interesting transition since it is the transition of the Sr^+ optical frequency standard. This transition has one magic wavelength at 1880 nm. This is caused by the increase in the $4d_{\frac{5}{2},m=\frac{3}{2}}$ polarizability as the photon energy approaches the $4d_{\frac{5}{2}} \rightarrow 5p_{\frac{3}{2}}$ excitation energy. The other three magic wavelengths lie close to 417 nm and are all caused by the rapid change in the $5s$ polarizability for photon energies lying between the excitation thresholds of the $5p_j$ doublet. The magic wavelength mainly arises from the cancellation of the $5p_{\frac{1}{2}}$ and $5p_{\frac{3}{2}}$ contributions to the $5s$ dynamic polarizability. These three magic wavelengths would allow the determination of the oscillator strength ratio $f_{5s\rightarrow 5p_{\frac{1}{2}}}:f_{5s\rightarrow 5p_{\frac{3}{2}}}$. This is similar to Ca^+[20,68], in which the magic wavelength of the $3d_{\frac{5}{2}} \rightarrow 4s_{\frac{1}{2}}$ clock transition lying between the transition wavelengths of the $4s \rightarrow 4p_j$ doublet was measured and the ratio of the oscillator strengths $f_{4s\rightarrow 4p_{\frac{1}{2}}}:f_{4s\rightarrow 4p_{\frac{3}{2}}}$ was determined with a deviation of less than 0.5%.

The dynamic polarizabilities of the $5s$ and $4d_{\frac{3}{2}}$ states are shown in Fig. 2(c), while Supplemental Table VII [31] lists the breakdown of the polarizabilities for the static case and at the magic wavelengths. This transition has one magic wavelength, at 1082 nm. This is caused by the increase in the $4d_{\frac{3}{2},m=\frac{3}{2}}$ polarizability as the photon energy approaches the $4d_{\frac{3}{2}} \rightarrow 5p_{\frac{3}{2}}$ excitation energy. Another magic wavelength (1005 nm) occurs at a slightly higher photon energy. It is caused by the rapid change of the $4d_{\frac{3}{2}}$ polarizability for photon energies lying between the excitation energies of the $4d_{\frac{3}{2}} \rightarrow 5p_j$ doublet. Combined with the experimental results for the $5s \rightarrow 5p_j$ oscillator strength, measurement of this magic wavelength would give an estimate of the oscillator strength ratio for $f_{4d_{\frac{3}{2}}\rightarrow 5p_{\frac{1}{2}}}:f_{4d_{\frac{3}{2}}\rightarrow 5p_{\frac{3}{2}}}$.

The other two magic wavelengths lie close to 417 nm and are both caused by the rapid change in the $5s$ polarizability for photon energies lying between the excitation thresholds of the $5s \rightarrow 5p_j$ doublet. Like the magic wavelength near 417 nm for the clock transition $5s \rightarrow 5d_{\frac{5}{2}}$, measurement of these two magic wavelengths would also allow determination of the oscillator strength ratio for the $5s \rightarrow 5p_{\frac{1}{2}}$ and $5s \rightarrow 5p_{\frac{3}{2}}$ transitions.

F. Uncertainties in the magic wavelength positions

An uncertainty analysis has been done for the magic wavelengths given in the preceding section. This analysis estimates how uncertainties in the matrix elements will translate into changes in the magic wavelengths. The motivation for this analysis is to define reasonable upper and lower limits on the wavelength, to assist an experimental search for these magic wavelengths.

For the $5s \rightarrow 5p_j$ polarizability differences, the matrix elements of $5s \rightarrow 5p_j$, $5p_j \rightarrow 5s$, $5p_j \rightarrow 4d_j$, $5p_j \rightarrow 6s$, and $5p_j \rightarrow 5d_j$ are dominant. For the $5s \rightarrow 4d_j$ polarizability differences, the $5s \rightarrow 5p_j$ and $4d_j \rightarrow 5p_j$ matrix elements are dominant. All these matrix elements were changed by 2% (as most of the reliable calculations and experiments agree with each other within a 2% difference) and the magic wavelengths were recomputed. The resultant difference is set as the uncertainty of the magic wavelength (as the uncertainties of these RCICP matrix elements are smaller than 0.75%, the uncertainty of the magic wavelength should be an overestimate). The matrix elements involving the different spin-orbit states of the same multiplet were all given the same scaling.

The uncertainties of each magic wavelength are listed in Table XI (and Supplemental Tables IV, V, VI and VII [31]). It is found that the magic wavelengths 764 nm for $5s \rightarrow 5p_{\frac{1}{2}}$, 709 nm for $5s \rightarrow 5p_{\frac{3}{2}m=\frac{1}{2}}$, 721 nm for $5s \rightarrow 5p_{\frac{3}{2}m=\frac{3}{2}}$, 1083 nm for $5s \rightarrow 4d_{\frac{3}{2}m=\frac{3}{2}}$, and 1880 nm for $5s \rightarrow 4d_{\frac{5}{2}m=\frac{3}{2}}$ are relatively sensitive to change in the matrix element. The uncertainties in the magic wavelength are from 4 to 133 nm. The reason is that the rate of change of $5s$ and $5p_j$ (or $4d_j$) polarizabilities is low near these magic wavelengths, namely, $d\alpha/d\omega$ is small. The magic wavelength calculated by Kaur *et al.* [65] using the RCC all-order method lies within our uncertainties.

Some of the magic wavelengths, however, such as those at 1009, 1004, and 417 nm, are relatively insensitive to the changes in the matrix elements. The magic wavelengths 1009 and 1004 nm lie in between the transition energies of the $5p_{\frac{3}{2}} \rightarrow 4d_j$ spin-orbit doublet. The magic wavelengths near 417 nm lie between the transition energies of the $5s \rightarrow 5p_j$ spin-orbit doublet. The present calculations of magic wavelengths agree excellently with the RCC all-order results of Kaur *et al.* [65].

Experimental determination of the oscillator strengths for the resonant $5s \rightarrow 5p_j$ transitions using a lifetime approach is complicated due to the existence of the $4d_j \rightarrow 5p_j$ transitions. However, the measurement of magic wavelengths near 417 nm for the $5s \rightarrow 4d_j$ transitions can give a reasonable estimate of the oscillator ratio of the two transitions of the $5s \rightarrow 5p_j$ doublet since the polarizability of the $5s$ state is so much larger than any of the other polarizabilities. The magic wavelength at 416.9999 nm changes by 0.0002 nm when the $4d_{\frac{5}{2}}$-$4f_j$ matrix elements are changed by 2%.

IV. CONCLUSION

The development and realization of a relativistic model potential description of quasi-single-electron atoms and ions have been presented. Rather than using a B-spline basis [69], single-electron spinors are expanded as a linear combination of S-spinors and L-spinors. The starting point of the calculation is a DF calculation for the core state. The DF wave functions then serve as the starting point for the calculations to describe

the ground and excited states of quasi-single-electron atoms or ions. The core electrons are kept frozen, where direct and exchange interactions between the valence electron and the core are computed without approximation. Dynamical interactions between the valence electron and the core beyond the DF level are incorporated through semiempirical polarization potentials.

The method is applied to the description of the low-lying states of Sr^+, giving line strengths and polarizabilities that are generally within 1%–2% of the significantly more computationally demanding relativistic all-order singles and doubles method [43,47]. A number of magic wavelengths are identified for the $5s \rightarrow 5p_{\frac{1}{2}}$, $5s \rightarrow 5p_{\frac{3}{2}}$, $5s \rightarrow 4d_{\frac{3}{2}}$, and $5s \rightarrow 4d_{\frac{5}{2}}$ transitions. We suggest that measurements of the 1009-nm magic wavelength for the $5s \rightarrow 5p_{\frac{3}{2}}$ transition would enable determination of the oscillator strength ratio of $f_{5p_{\frac{3}{2}} \rightarrow 4d_{\frac{3}{2}}} : f_{5p_{\frac{3}{2}} \rightarrow 4d_{\frac{5}{2}}}$. Determination of the magic wavelengths for the $5s \rightarrow 4d_{\frac{3}{2}}$ and $5s \rightarrow 4d_{\frac{5}{2}}$ transitions near 417 nm would allow determination of the oscillator strength ratio for the $5s \rightarrow 5p_{\frac{1}{2}}$ and $5s \rightarrow 5p_{\frac{3}{2}}$ transitions.

This approach can also be used for a variety of heavy atoms or ions, such as Cs, Ba^+, and Yb^+. Atomic properties, including the energy levels, the oscillator strengths, the static and dynamic multipole polarizabilities, the black-body radiation shifts, and the dispersion coefficients that characterize the long-range interaction between pairs of atoms, can be studied with improved accuracy compared to our previous non-relativistic-based CICP treatment [6].

ACKNOWLEDGMENTS

The authors would like to thank Prof. Ulyana Safronova for providing tables of reduced matrix elements for Sr^+. We would also like to thank Prof. Fumihiro Koike and an anonymous referee for their valuable suggestions. This research was partially supported by Australian Research Council (ARC) Discovery Project DP1092620. The work of J.J. was supported by National Natural Science Foundation of China (NSFC) Grants No.11147018 and No. 11564036, and Y.C. was supported by NSFC Grant No.11304063. The work of M.W.J.B. was supported by an ARC Future Fellowship (FT100100905).

[1] H. M. Quiney, I. P. Grant, and S. Wilson, J. Phys. B **22**, L15 (1989).
[2] I. P. Grant and H. M. Quiney, Phys. Rev. A **62**, 022508 (2000).
[3] I. P. Grant, *Relativistic Quantum Theory of Atoms and Molecules Theory and Computation* (Springer, New York, 2007).
[4] J. Mitroy, D. C. Griffin, D. W. Norcross, and M. S. Pindzola, Phys. Rev. A **38**, 3339 (1988).
[5] J. Mitroy, J. Phys. B **26**, 3703 (1993).
[6] J. Mitroy and M. W. J. Bromley, Phys. Rev. A **68**, 052714 (2003).
[7] J. Migdalek and W. E. Baylis, J. Phys. B **11**, L497 (1978).
[8] J. Mitroy, Phys. Rev. A **78**, 052515 (2008).
[9] S. R. Lundeen, Adv. At. Mol. Opt. Phys. **52**, 161 (2005).
[10] R. A. Komara, M. A. Gearba, C. W. Fehrenbach, and S. R. Lundeen, J. Phys. B **38**, S87 (2005).
[11] M. S. Safronova, S. G. Porsev, M. G. Kozlov, and C. W. Clark, Phys. Rev. A **85**, 052506 (2012).
[12] J. Mitroy and M. S. Safronova, Phys. Rev. A **79**, 012513 (2009).
[13] M. S. Safronova, M. G. Kozlov, and C. W. Clark, Phys. Rev. Lett. **107**, 143006 (2011).
[14] S. G. Porsev, M. S. Safronova, and M. G. Kozlov, Phys. Rev. A **85**, 062517 (2012).
[15] J. Migdalek and W. E. Baylis, J. Phys. B **17**, L459 (1984).
[16] J. Migdalek and W. E. Baylis, J. Phys. B **19**, 1 (1986).
[17] J. Migdalek and W. E. Baylis, Z. Phys. D **27**, 9 (1993).
[18] J. Migdalek and A. Glowacz-Proszkiewicz, J. Phys. B **40**, 4143 (2007).
[19] J. Migdałek, Can. J. Phys. **54**, 118 (1976).
[20] L. Y. Tang, M. W. J. Bromley, Z. C. Yan, and J. Mitroy, Phys. Rev. A **87**, 032507 (2013).
[21] J. Mitroy, Aust. J. Phys. **52**, 973 (1999).
[22] J. Mitroy, M. S. Safronova, and C. W. Clark, J. Phys. B **43**, 202001 (2010).
[23] P. Dubé, A. A. Madej, M. Tibbo, and J. E. Bernard, Phys. Rev. Lett. **112**, 173002 (2014).
[24] A. A. Madej, P. Dubé, Z. Zhou, J. E. Bernard, and M. Gertsvolf, Phys. Rev. Lett. **109**, 203002 (2012).
[25] A. D. Ludlow, M. M. Boyd, J. Ye, E. Peik, and P. O. Schmidt, Rev. Mod. Phys. **87**, 637 (2015).
[26] S. Kaneko, J. Phys. B **10**, 3347 (1977).
[27] E. Clementi and C. Roetti, At. Data Nucl. Data Tables **14**, 177 (1974).
[28] F. A. Parpia, C. Froese Fischer, and I. P. Grant, Comp. Phys. Commun. **94**, 249 (1996).
[29] P. Jönsson, G. Gaigalas, J. Bieroń, C. F. Fischer, and I. P. Grant, Comput. Phys. Commun. **184**, 2197 (2013).
[30] O. Zatsarinny and C. Froese Fischer, Comput. Phys. Commun. **202**, 287 (2016).
[31] See Supplemental Material at http://link.aps.org/supplemental/10.1103/PhysRevA.94.062514 for additional tables of basis exponents and breakdowns of polarizabilities at the magic wavelengths.
[32] M. W. J. Bromley and J. Mitroy, Phys. Rev. A **65**, 012505 (2001).
[33] M. Abramowitz and I. E. Stegun (eds.), *Handbook of Mathematical Functions, Natl. Bur. Stand. Appl. Math. Ser. 55* (U.S. Government Printing Office, Washington, DC, 1972).
[34] J. Mitroy, J. Y. Zhang, and M. W. J. Bromley, Phys. Rev. A **77**, 032512 (2008).
[35] D. E. Kelleher and L. I. Podobedova, J. Phys. Chem. Ref. Data **37**, 267 (2008).
[36] P. J. Mohr, D. B. Newell, and B. N. Taylor, Rev. Mod. Phys. **88**, 035009 (2016).
[37] D. Baye, L. Filippin, and M. Godefroid, Phys. Rev. E **89**, 043305 (2014).
[38] A. Kramida, Y. Ralchenko, J. Reader, and NIST ASD Team, *NIST Atomic Spectra Database*, v5.0.0 (NIST, Boulder, CO, 2012).
[39] L. Y. Tang, Y. H. Zhang, X. Z. Zhang, J. Jiang, and J. Mitroy, Phys. Rev. A **86**, 012505 (2012).

[40] L. Filippin, M. Godefroid, and D. Baye, Phys. Rev. A **90**, 052520 (2014).
[41] R. Szmytkowski and G. Łukasik, Phys. Rev. A **93**, 062502 (2016).
[42] W. R. Johnson, D. Kolb, and K. Huang, At. Data Nucl. Data Tables **28**, 333 (1983).
[43] U. I. Safronova, Phys. Rev. A **82**, 022504 (2010).
[44] S. Hameed, A. Herzenberg, and M. G. James, J. Phys. B **1**, 822 (1968).
[45] S. Hameed, J. Phys. B **5**, 746 (1972).
[46] J. Migdalek, J. Phys. B **49**, 185004 (2016).
[47] D. Jiang, B. Arora, M. S. Safronova, and C. W. Clark, J. Phys. B **42**, 154020 (2009).
[48] R. Pal, M. S. Safronova, W. R. Johnson, A. Derevianko, and S. G. Porsev, Phys. Rev. A **75**, 042515 (2007).
[49] M. S. Safronova and W. R. Johnson, Adv. At. Mol. Opt. Phys. **55**, 191 (2008).
[50] L. W. Wansbeek, B. K. Sahoo, R. G. E. Timmermans, B. P. Das, and D. Mukherjee, Phys. Rev. A **78**, 012515 (2008).
[51] L. W. Wansbeek, B. K. Sahoo, R. G. E. Timmermans, B. P. Das, and D. Mukherjee, Phys. Rev. A **82**, 029901(E) (2010).
[52] M. S. Safronova and U. I. Safronova, Phys. Rev. A **83**, 012503 (2011).
[53] J. Mitroy, J. Y. Zhang, and K. Varga, Phys. Rev. Lett. **101**, 123201 (2008).
[54] E. Biémont, J. Lidberg, S. Mannervik, L.-O. Norlin, P. Royen, A. Schmitt, W. Shi, and X. Tordoir, Eur. Phys. J. D **11**, 355 (2000).
[55] B. K. Sahoo, Md. R. Islam, B. P. Das, R. K. Chaudhuri, and D. Mukherjee, Phys. Rev. A **74**, 062504 (2006).
[56] A. A. Madej and J. D. Sankey, Opt. Lett. **15**, 634 (1990).
[57] S. Mannervik, J. Lidberg, L.-O. Norlin, P. Royen, A. Schmitt, W. Shi, and X. Tordoir, Phys. Rev. Lett. **83**, 698 (1999).
[58] V. Letchumanan, M. A. Wilson, P. Gill, and A. G. Sinclair, Phys. Rev. A **72**, 012509 (2005).
[59] P. Kuske, N. Kirchner, W. Wittmann, H. J. Andra, and D. Kaiser, Phys. Lett. **64**, 377 (1978).
[60] E. H. Pinnington, R. W. Berends, and M. Lumsden, J. Phys. B **28**, 2095 (1995).
[61] J. Kaur, D. K. Nandy, B. Arora, and B. K. Sahoo, Phys. Rev. A **91**, 012705 (2015).
[62] D. J. Margoliash and W. J. Meath, J. Chem. Phys. **68**, 1426 (1978).
[63] A. Kumar and W. J. Meath, Mol. Phys. **54**, 823 (1985).
[64] J. Nunkaew, E. S. Shuman, and T. F. Gallagher, Phys. Rev. A **79**, 054501 (2009).
[65] J. Kaur, S. Singh, B. Arora, and B. K. Sahoo, Phys. Rev. A **92**, 031402 (2015).
[66] B. K. Sahoo, R. G. E. Timmermans, B. P. Das, and D. Mukherjee, Phys. Rev. A **80**, 062506 (2009).
[67] M. S. Safronova, D. Jiang, B. Arora, C. W. Clark, M. G. Kozlov, U. I. Safronova, and W. R. Johnson, IEEE Trans. Ultrason. Ferroelectr. Freq. Control **57**, 94 (2010).
[68] P.-L. Liu, Y. Huang, W. Bian, H. Shao, H. Guan, Y.-B. Tang, C.-B. Li, J. Mitroy, and K.-L. Gao, Phys. Rev. Lett. **114**, 223001 (2015).
[69] W. R. Johnson, S. A. Blundell, and J. Sapirstein, Phys. Rev. A **37**, 307 (1988).